Cryo-EM structure of human mitochondrial trifunctional protein

Kai Liang[a,b,c,1], Ningning Li[c,d,e,1], Xiao Wang[c,f], Jianye Dai[c,g], Pulan Liu[a,c,d], Chu Wang[c,g], Xiao-Wei Chen[c,f], Ning Gao[c,d,e], and Junyu Xiao[a,c,d,2]

[a]State Key Laboratory of Protein and Plant Gene Research, Peking University, 100871 Beijing, China; [b]Academy for Advanced Interdisciplinary Studies, Peking University, 100871 Beijing, China; [c]Peking-Tsinghua Center for Life Sciences, Peking University, 100871 Beijing, China; [d]School of Life Sciences, Peking University, 100871 Beijing, China; [e]State Key Laboratory of Membrane Biology, Peking University, 100871 Beijing, China; [f]Institute of Molecular Medicine, Peking University, 100871 Beijing, China; and [g]College of Chemistry and Molecular Engineering, Peking University, 100871 Beijing, China

Edited by Robert M. Glaeser, Lawrence Berkeley National Laboratory, Berkeley, CA, and approved May 25, 2018 (received for review January 23, 2018)

The mitochondrial trifunctional protein (TFP) catalyzes three reactions in the fatty acid β-oxidation process. Mutations in the two TFP subunits cause mitochondrial trifunctional protein deficiency and acute fatty liver of pregnancy that can lead to death. Here we report a 4.2-Å cryo-electron microscopy α2β2 tetrameric structure of the human TFP. The tetramer has a V-shaped architecture that displays a distinct assembly compared with the bacterial TFPs. A concave surface of the TFP tetramer interacts with the detergent molecules in the structure, suggesting that this region is involved in associating with the membrane. Deletion of a helical hairpin in TFPβ decreases its binding to the liposomes in vitro and reduces its membrane targeting in cells. Our results provide the structural basis for TFP function and have important implications for fatty acid oxidation related diseases.

fatty acid β-oxidation | mitochondrial trifunctional protein | cryo-EM

The β-oxidation pathway breaks down fatty acid molecules to generate energy and plays a pivotal role in human metabolism. Four enzymatic steps operate successively during this process: (*i*) fatty acyl-CoA is dehydrogenated to produce 2,3-Enoyl-CoA; (*ii*) water is added to the double bond of 2,3-enoyl-CoA, yielding 3-hydroxyacyl-CoA; (*iii*) 3-hydroxyacyl-CoA is again dehydrogenated to form 3-ketoacyl-CoA; and (*iv*) 3-ketoacyl-CoA is thiolyzed between the α- and β-carbons to remove a two-carbon unit, which is released in the form of acetyl-CoA (Fig. 1*A*). These four steps are repeated until all carbons in the fatty acyl-CoA are turned into acetyl-CoA, which enters the citric acid cycle. The majority of fatty acid β-oxidation occurs in mitochondria. The first step is catalyzed by several acyl-CoA dehydrogenases, each with a preference for different fatty acyl chain lengths. The last three steps are mainly catalyzed by the mitochondrial trifunctional protein (TFP or MTP; also known as the trifunctional enzyme, TFE), a protein complex attached to the inner mitochondrial membrane (1).

TFP has two subunits. The alpha subunit (TFPα), encoded by the HADHA gene, comprises the 2,3-enoyl-CoA hydratase (ECH) and 3-hydroxyacyl-CoA dehydrogenase (HACD) activities. The beta subunit (TFPβ), encoded by the HADHB gene, contains the thiolase activity. Mutations in these two subunits that result in the loss of TFP function cause mitochondrial trifunctional protein deficiency (MTPD), an autosomal recessive disorder manifesting a wide range of clinical presentations, including liver dysfunction, retina abnormality, muscle atrophy, cardiomyopathy, and sudden death (2, 3). Mutations in TFPα that specifically abolish the HACD activity can also lead to acute fatty liver of pregnancy (AFLP), a life-threatening condition caused by the accumulation of undermetabolized fatty acids in the fetus, which are disposed into the maternal circulation and overburden the mother's metabolic capacity (4–6). On the other hand, pharmacological perturbation of TFP activity may be desirable under certain conditions. Trimetazidine, a drug used to treat angina, has been shown to exert its effects by targeting TFPβ (7, 8). It is proposed that by blocking TFP function, trimetazidine shifts cellular metabolism to glucose utilization, thereby reducing oxygen consumption and preserving cardiac cells during ischemia (7), although this mechanism is still under debate (9, 10). Excessive fatty acid oxidation has also been linked to cachexia, a severe muscle-wasting disorder in patients with advanced cancer, and pharmacological inhibition of the β-oxidation pathway relieved muscle damage in animal models (11).

The structure of human TFP is not yet available despite its functional importance. Crystal structures of two bacterial TFPs from *Pseudomonas fragi* (pfTFP) and *Mycobacterium tuberculosis* (mtTFP) have been determined (12, 13); however, the two subunits of human TFP display limited sequence identities to the bacterial homologs and contain several insertion regions that are specific to eukaryotic TFPs. The bacterial TFPs form heterotetramers with two alpha and two beta chains; however, it is generally believed that the human TFP functions as an α4β4 octamer. Furthermore, the bacterial TFPs are soluble proteins, whereas the human TFP is associated with the inner mitochondrial membrane, although the membrane targeting mechanism is unclear. Here we

Significance

The β-oxidation is a fundamental metabolic pathway that breaks down fatty acid molecules to generate energy. The mitochondrial trifunctional protein (TFP) catalyzes three reactions during this process, and mutations in the TFP subunits cause diseases such as mitochondrial trifunctional protein deficiency and acute fatty liver of pregnancy. Despite the fact that the reactions catalyzed by the TFP are well documented in almost all major biochemistry textbooks, the structure of the human TFP is not yet known. Here using the cryo-EM single-particle reconstruction method, we have determined a 4.2-Å structure of the human TFP. Our results provide insights into the function of an important enzyme complex and shed light on the molecular pathology of human fatty acid oxidation disorders.

Author contributions: J.X. designed research; K.L., N.L., X.W., J.D., P.L., and J.X. performed research; C.W. and X.-W.C. contributed new reagents/analytic tools; K.L., N.L., X.W., J.D., P.L., C.W., X.-W.C., N.G., and J.X. analyzed data; and K.L., N.L., N.G., and J.X. wrote the paper.

The authors declare no conflict of interest.

This article is a PNAS Direct Submission.

Data deposition: EM maps have been deposited in the Electron Microscopy Data Bank under accession codes EMD-6940 (TFP tetramer), EMD-6945 (TFP tetramer, with detergent), and EMD-6944 (TFP octamer). Pseudoatomic models of the TFP tetramer and octamer have been deposited in the Protein Data Bank, www.pdb.org (PDB ID codes 5ZQZ and 5ZRV).

[1]K.L. and N.L. contributed equally to this work.

[2]To whom correspondence should be addressed. Email: junyuxiao@pku.edu.cn.

This article contains supporting information online at www.pnas.org/lookup/suppl/doi:10.1073/pnas.1801252115/-/DCSupplemental.

Published online June 18, 2018.

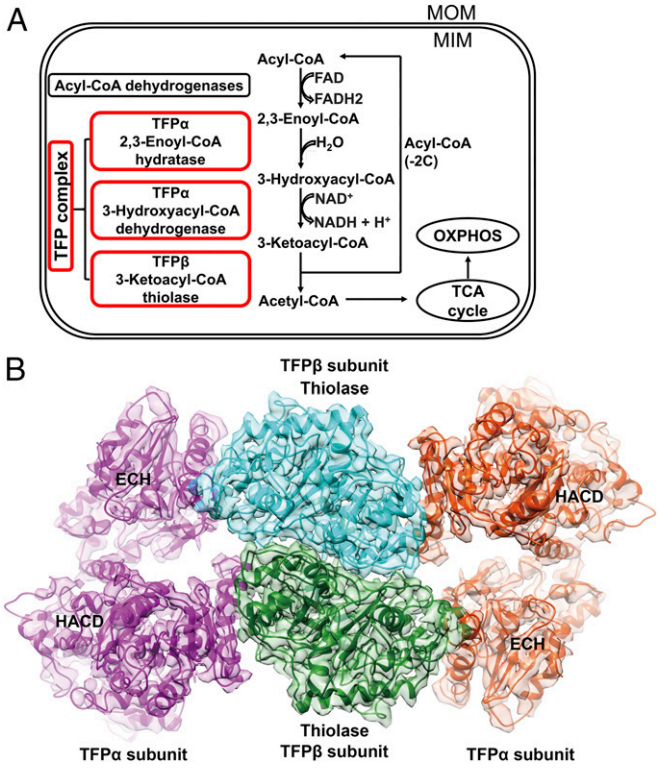

Fig. 1. Cryo-EM structure of the human TFP complex. (*A*) Schematic diagram of the mitochondrial fatty acid β-oxidation pathway. MOM, mitochondrial outer membrane; MIM, mitochondrial inner membrane; OXPHOS, oxidative phosphorylation. (*B*) The cryo-EM density map of the human TFP complex. The two TFPα subunits are shown in magenta and orange, and the two TFPβ subunits are shown in cyan and green.

present a 4.2-Å cryo-EM structure of human TFP to provide a structural glimpse of this important metabolic enzyme complex. Our results reveal that the basic architecture of the human TFP is also an α2β2 heterotetramer; nevertheless, the interaction between the alpha and beta subunits in the tetramer are fundamentally different compared with that in the prokaryotic TFPs. A helical hairpin in TFPβ is involved in interacting with the detergent molecules, and our in vitro and in vivo data suggest that it plays an important role in the membrane association of TFPβ. We also determined an octameric TFP structure at 7.7-Å resolution, which raises the possibility of functional regulation by higher-order oligomerization. Lastly, the structure allowed the structural mapping of known pathogenic missense mutations and examination of their potential impacts. Together, our results provide important information for understanding human TFP function and related diseases.

Results and Discussion

Structure Determination of the Human TFP. We coexpressed the two subunits of human TFP in *Escherichia coli* and purified the complex (*SI Appendix*, Fig. S1 *A* and *B*) using a procedure similar to the method established by Arlaud and coworkers (10). One major change is that we used dodecyl-β-D-maltoside (DDM) instead of octyl-β-D-glucoside (β-OG) in the buffer, which is crucial to prepare the sample for cryo-EM study. The purified TFP efficiently converts 2,3-enoyl-palmitoyl-CoA to acetyl-CoA, suggesting that it is enzymatically active (*SI Appendix*, Fig. S1*C*). We then collected 4,929 micrographs on a Titan Krios transmission electron microscope equipped with a K2 Summit direct electron detector and determined a tetrameric TFP structure at an overall resolution of 4.2 Å (*SI Appendix*, Fig. S2). The majority of the map displays a resolution better than 4 Å (*SI Appendix*, Fig. S2*F*). The initial models of TFPα and TFPβ were generated using the bacterial homologs as templates and docked into the EM map. Most of the secondary structures fit into the map well, and some bulky side chains can be clearly identified (*SI Appendix*, Fig. S3). Guided by these structural features, we were able to build a near-complete pseudoatomic model of the TFP complex (*SI Appendix*, Table S1). Residues 261–265 and 637–647 in TFPα and residues 187–192 in TFPβ were not built, due to the lack of densities in these regions.

Structure of the Human TFP α2β2 Tetramer. The cryo-EM structure of the human TFP complex reveals an unambiguous α2β2 heterotetramer (Figs. 1*B* and 2*A*). Two TFPβ molecules form a homodimer that is located in the middle, and two TFPα molecules are mounted on the side like two wings. There is no interaction between the two TFPα molecules. The overall structure of TFPα is similar to the alpha subunits of pfTFP and mtTFP (*SI Appendix*, Fig. S4 *A–C*). The ECH and HACD domains are located at the N-terminal and C-terminal halves, respectively. Residues 224–236 in the ECH domain are absent in the bacterial homologs (*SI Appendix*, Figs. S4 *A* and S5). This region forms a loop between the A5 β-strand and the H7 α-helix (for ease of structural comparison, we will describe the secondary structures following the mtTFP nomenclature) (13) and plays an important role in interacting with TFPβ in the human TFP (Fig. 2*A*). TFPβ adopts a classical thiolase fold (*SI Appendix*, Fig. S4 *D–F*). Two regions in human TFPβ are unique (*SI Appendix*, Figs. S4*D* and S6). Residues 173–220 form a helical hairpin (referred to as TFPβ_HH hereafter) between the NB4 strand and the LA2 helix and is important for the membrane association of TFPβ (see below). Residues 395–408, located between the CA2 and CA3 helices, are involved in interacting with TFPα to mediate the tetramer formation (Fig. 2*A*).

Human TFP, pfTFP, and mtTFP all form tetrameric assemblies; however, the quaternary structures of these tetramers are different (Fig. 2). The TFPβ dimers are similar and function as the central scaffold for the tetramer formation in all three complexes, but the alpha subunits are placed in distinct manners. In the pfTFP tetramer, only the ECH domains of the alpha subunits interact with the TFPβ dimer (Fig. 2*B*). The HACD domains interact with each other via a helical hairpin consisting of the CH2A and CH2B helices, resulting in the formation of a closed ring-like tetramer. In the mtTFP tetramer, however, the TFPα molecules undergo ∼96° rotations around the TFPβ dimer, and both the ECH and HACD domains of mtTFPα are involved in interacting with mtTFPβ (Fig. 2*C*). The HACD domains of mtTFPα do not touch each other, and the CH2A-CH2B helical hairpins are exposed to the solvent. As a result, an open V-shaped tetramer is created. Despite these large differences, how the alpha subunits face the beta subunits remains similar in the two complexes in a general manner, and the H9A helices in the ECH domains of the alpha subunits are involved in interacting with the beta subunits in both of them (Fig. 2 *B* and *C*). At first glance, the human TFP tetramer resembles the mtTFP, also featuring a V-shaped architecture (Fig. 2*A*). Nevertheless, the orientations of the alpha subunits are completely different. Compared with the TFPα molecules in the mtTFP, the two TFPα subunits in the human TFP are mounted onto the TFPβ dimer in inverted manners, such that the relative positions of the ECH and HACD domains are swapped with respect to the TFPβ dimer (Fig. 2 *A* and *C*). The H9A helices face the solvent and make no contact with TFPβ (Fig. 2*A*). Instead, the CH2A-CH2B helical hairpins in the HACD domains play critical roles in engaging with TFPβ. These different quaternary structures suggest that these TFP complexes would have distinct substrate channeling paths (Fig. 2) and are consistent with the results of a previous phylogenetic analysis showing that these proteins belong to different TFP subfamilies (13). Obviously, these TFPs have long diverged from each other during evolution.

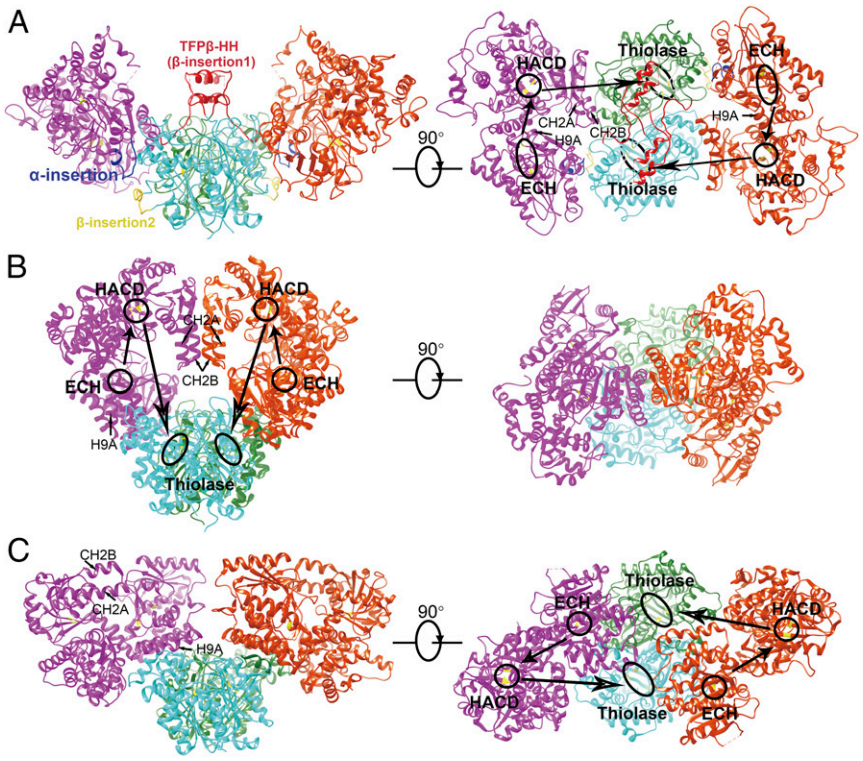

Fig. 2. Different quaternary structures of human TFP, pfTFP, and mtTFP. (*A*) The human TFP tetramer shown in two orientations. The insertion region in the ECH domain of TFPα is colored blue; and the two insertions in TFPβ are colored yellow and red. The CH2A–CH2B helical hairpin and the H9A helix are indicated. The active sites of TFPα (ECH: Glu151, Glu173; HACD: His498, Glu510) and TFPβ (Cys138, His428, Cys458) are indicated with black circles. The directions of how the substrate is presumably transferred between the three active sites are illustrated with arrows. (*B*) The structure of pfTFP [Protein Data Bank (PDB) ID code 1WDK] shown in the same orientations and color schemes as the human TFP in *A*. (*C*) The structure of mtTFP (PDB ID code 4B3H).

TFPβ_HH Is Involved in the Membrane Association of TFPβ. Human TFP is attached to the inner mitochondria membrane, despite the fact that neither TFPα nor TFPβ has a predicted transmembrane helix. Interestingly, our cryo-EM map reveals noncontinuous densities below the concave surface of the α2β2 tetramer, which could be attributed to the detergent molecules (Fig. 3*A*). The inner mitochondrial membrane is extensively curved and contains many cristae that protrude toward the matrix, and we envision that TFP could use this concave surface to localize to the cristae region. A close examination of the electrostatic property of this concave surface reveals several positively charged patches (*SI Appendix*, Fig. S7*A*), formed by residues including Lys254, Lys259, Arg260, Lys267, Lys284, Lys292, Lys569, Arg630, Lys631, and Lys634 from TFPα, and Arg174, Arg177, Arg180, and Arg195 from the TFPβ_HH region in TFPβ. Notably, these residues are largely conserved among the eukaryotic TFP homologs (*SI Appendix*, Fig. S7 *B* and *C*).

TFPβ_HH from the two TFPβ molecules cross each other and face the detergent micelle (Fig. 3*A*). To assess whether this region contributes to the membrane association of TFPβ, we constructed TFPβ_Δ173–208, which has the TFPβ_HH removed. As separate expression of TFPβ led to aggregations (10), we coexpressed TFPα and TFPβ_Δ173–208 to generate a mutant TFP. Importantly, this mutant TFP is eluted from the size exclusion column at a position similar to the wild-type (WT) TFP (*SI Appendix*, Fig. S1*D*), suggesting that deletion of TFPβ_HH does not significantly compromise the integrity of the TFP complex. We then performed in vitro liposome binding experiments (Fig. 3*B*). WT TFP directly associates with the cardiolipin-containing liposomes, as both TFPα and TFPβ are mainly detected in the liposome-enriched top layers after centrifugation. When the mutant TFP is assayed at the same condition, TFPα remains attached to the liposomes, while TFPβ_Δ173–208 displays significantly reduced binding. These data suggest that TFPα can bind to the liposomes independent of TFPβ. Unlike TFPβ, TFPα is stable on its own, and purified TFPα indeed binds to the liposomes strongly by itself (Fig. 3*B*). These data also suggest that deletion of TFPβ_HH decreased its interaction with the lipid molecules, and TFPβ_Δ173–208 in the mutant TFP is still partially associated with the liposome likely because of its association with TFPα.

To further investigate the membrane association of the two TFP subunits in cells, we transfected HEK293A cells with V5-tagged TFPα and Flag-tagged TFPβ. We then isolated mitochondria from these cells and separated the mitochondria membranes. Consistent with the liposome-binding experiments, TFPα is capable of localizing to the mitochondrial membrane by itself (Fig. 3*C*). TFPβ is not stable when expressed alone, as only a degradation band was detected in the mitochondria lysates. When coexpressed with TFPα, TFPβ is stabilized and is predominantly enriched in the mitochondria membrane fraction (Fig. 3*C*). In contrast, significant amounts of TFPβ_Δ173–208 become soluble. Together, these results suggest that TFPα is an intrinsic mitochondrial membrane protein. The membrane targeting of TFPβ likely relies on both its interaction with TFPα and the TFPβ_HH region. The fact that eliminating the TFPβ_HH region reduces the binding of TFPβ to the liposome/membrane suggests that the TFP complex is likely attached to the inner mitochondrial membrane using the concave surface revealed in the structure.

The TFP Octamer. Historically, the TFP complex purified from rat liver has an estimated molecular weight of 460 kDa; thus the mammalian TFP is proposed to be a heterooctamer with an α4β4 stoichiometry (14). This view is commonly held and is documented in several major biochemistry textbooks (15, 16). Nevertheless, there is a discrepancy between different studies in the literature as to whether the TFP is an α2β2 tetramer or an α4β4 octamer, since analyses supporting either form have been reported, and sometimes both states have been observed at the same time (8, 10, 14, 17–19). In our study, particles corresponding to both the α2β2 tetramers and the α4β4 octamers were found, with a ∼2:1 ratio (*SI Appendix*, Fig. S2*C*). Nevertheless, the octamers are not stable and display a high degree of conformation heterogeneity. We analyzed 388,480 such particles and determined an α4β4 octamer structure

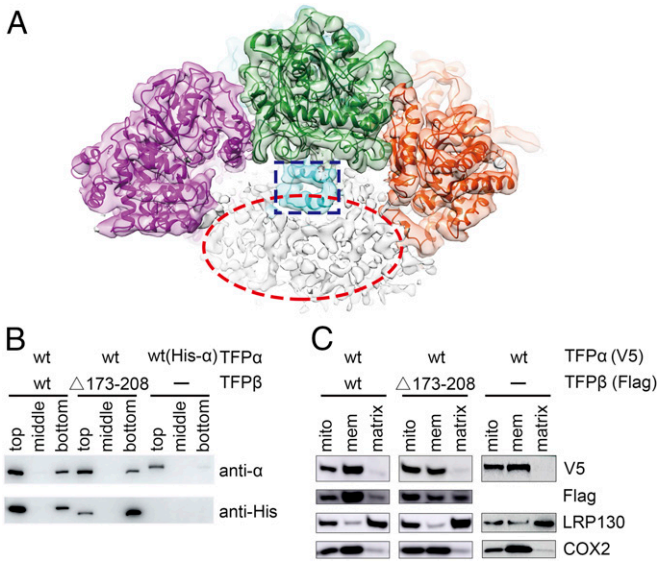

Fig. 3. TFPβ_HH is involved in the membrane association of TFPβ. (*A*) The cryo-EM density map before the detergent-free mask is applied, with the structure model docked into the map. The TFPβ_HH regions in TFPβ are highlighted with a blue rectangle. The noncontinuous density shown in the red oval below the TFP tetramer presumably corresponds to the detergent molecules. (*B*) TFPβ_HH is important for the liposome binding of TFPβ. Cardiolipin-containing liposomes were mixed with the indicated proteins and incubated for 1 h, before the addition of Optiprep reagent to a final concentration of 35%. After centrifugation, 200-μL aliquots were taken out from different layers, from top to bottom, and analyzed by Western blot using an anti-TFPα antibody and an anti-His antibody that recognizes the His tag on TFPβ. Liposomes are enriched in the top layers after centrifugation. (The TFPα in the WT and mutant TFP complexes are untagged and therefore appear smaller on the gel compared with the His-tagged TFPα.) (*C*) TFPβ_HH is important for the membrane association of TFPβ in cells. C-terminally V5-tagged TFPα and C-terminally Flag-tagged TFPβ were expressed in HEK293A cells as indicated. The mitochondria of these cells were isolated, and the soluble proteins were separated from the mitochondria membranes by sonication and ultracentrifugation. COX2 is an inner mitochondrial membrane protein, and LRP130 is a mitochondrial matrix protein. Mito, mitochondria; mem, membrane.

at 7.7 Å from a small population of particles (*SI Appendix*, Figs. S2 and S8*A*). The octamer is formed by two tetramers, with their concave surfaces facing each other (*SI Appendix*, Fig. S8 *B* and *C*). The two tetramers display a ∼48° twist when viewed from the convex side and are not parallel to each other (*SI Appendix*, Fig. S8*B*). Interestingly, not much protein–protein interaction is observed between the two tetramers. The only direct contacts between the two tetramers are seen between the TFPα molecules, mediated by the H7–H8 loop in the ECH domain (*SI Appendix*, Fig. S8 *C* and *D*). The two tetramers appear to be mainly glued together by a detergent micelle (*SI Appendix*, Fig. S8*C*). The mammalian TFPs are membrane associated, and therefore require the presence of detergents to be stabilized in vitro. The nature and strength of the detergents used during purification may affect the oligomeric states of TFP, providing a plausible explanation for the inconsistent conclusions drawn in previous studies. Since there is no extensive protein–protein interaction between the two tetramers, the functional significance of the octamer is not apparent, and we cannot rule out the possibility that it is a protein purification artifact. On the other hand, this higher-order organization could be conveniently used by the cell to regulate the access of the TFP tetramer to the inner mitochondria membrane.

Implications for Diseases. A plethora of mutations in TFPα and TFPβ have been reported to cause human diseases. Besides the deletion, nonsense, and frame-shift mutations that lead to the complete loss of individual subunits, a large number of missense mutations have also been identified (Fig. 4*A* and *SI Appendix*, Tables S2 and S3). Most of these mutations occur at low frequencies. E510Q in TFPα is by far the most common disease mutant, causing long-chain 3-hydroxyacyl-CoA dehydrogenase deficiency and AFLP (5, 6, 20–23). Glu510 is part of the His–Glu catalytic dyad in the active site of HACD (24); and substituting this critical residue by a Gln would abolish HACD activity and jam the β-oxidation cycle at the third step. Besides E510Q, some other mutations are found in the active sites of TFPα and TFPβ as well. For example, Gly148 in TFPα aligns with Gly116 in mtTFPα and is involved in forming the oxyanion hole in the ECH domain that binds the thioester oxygen of the fatty acyl-CoA during the hydration reaction (13). The G148R mutant found in a patient (25) would disturb the structural geometry of this region and interfere with catalysis. Similarly, His379 in TFPβ is also an important active site residue that functions to stabilize the fatty acyl-CoA during the thiolysis reaction. Only a His or an Asn is allowed at this position (26), and the H379R patient mutant (27) would eliminate TFPβ function. Other mutations appear to impact the structural stability of TFP. For example, Arg235 in TFPα appears to make hydrogen bonds with the LA2 helix in TFPβ (Fig. 4*B*), and the R235W mutant found in two studies (25, 28) might destabilize the TFPα–TFPβ interaction. Notably, Arg235 is located in a region that is not present in the bacterial homologs (see above); thus, it would not be possible to evaluate the mutation effect of this residue without the human TFP structure. Arg676 in TFPα is frequently mutated (5, 25, 29, 30) and is well resolved in our structure (Fig. 4*C*). It appears to make a hydrogen bond with the main chain carbonyl group of Arg732, and its mutation would result in the loss of this

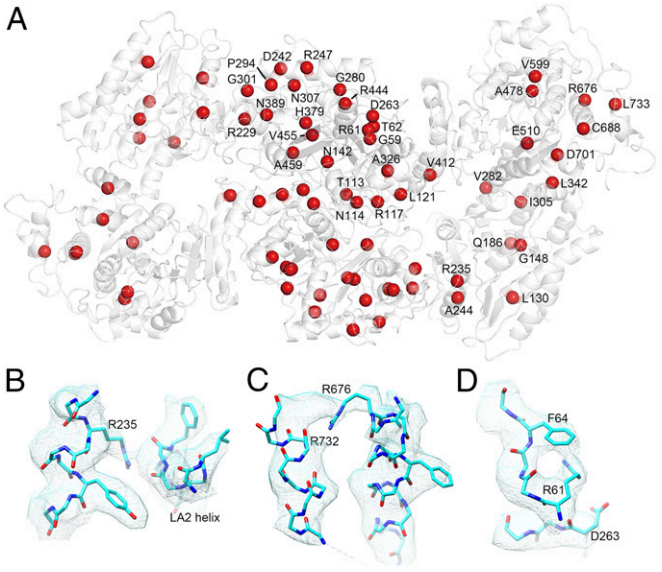

Fig. 4. TFP residues mutated in patients. (*A*) The TFP structure is shown as white ribbons. The Cα atoms of the TFP residues that are mutated in patients are shown as red spheres. The missense mutations found in TFPα include L130P, G148R, Q186E, R235W, A244V, V282D, I305N, L342P, V412L, A478P, A478V, E510Q, V599M, R676C, R676H, R676L, C688Y, D701G, and L733P. The missense mutations found in TFPβ include G59D, R61C, R61H, T62A, N114D, N114S, R117G, L121P, T133P, N142K, R229L, D242G, R247C, R247H, D263G, G280D, P294L, P294R, G301S, G301D, N307D, A326P, H379R, N389D, R444K, V455G, and A459E. Among them, TFPα-E510Q is the most common mutant. (*B*) Arg235 in TFPα appears to make hydrogen bonds with the LA2 helix in TFPβ. The electron density map is shown as light blue meshes. (*C*) Arg676 in TFPα appears to make a hydrogen bond with the main chain carbonyl group of Arg732. (*D*) Arg61 in TFPβ likely interacts with Phe64 and Asp263.

interaction. Similarly, Arg61 in TFPβ is often found to be mutated (29, 31, 32) and has clear density in our structure (Fig. 4*D*). The side chain of this Arg is located inside TFPβ and is involved in making a cation-π interaction with Phe64 and likely a salt bridge interaction with Asp263. Changing this Arg to a Cys or a His, or changing Asp263 to a Gly found in several other patients (31, 32), would all lead to destabilization of TFPβ. In the upcoming era of "precision medicine," more mutations are likely to be detected within this clinically important molecular machinery, and our structure provides a framework for evaluating their effects.

In summary, we have determined a near-atomic resolution cryo-EM structure of the human mitochondrial trifunctional protein, which displays distinctive structural features and a different quaternary assembly compared with the bacterial homologs. A helical hairpin in the TFPβ is important for its membrane association. Our results provide the long-sought-after structure information for an essential metabolic enzyme complex and shed light on the molecular pathology of human fatty acid oxidation disorders.

Materials and Methods

Expression and Purification of the TFP Complex. For purification of the TFP complex, human TFPα (residues 37–763) and TFPβ (residues 34–474) were coexpressed in *E. coli* Rosetta (DE3), with an 8xHis tag fused to the N termini of TFPβ. For purification of TFPα alone, the 8xHis tag is fused to the N termini of TFPα. The culture was grown at 37 °C to an OD_{600} of 1.0 and induced by the addition of 0.1 mM isopropyl β-D-thiogalactoside at 23 °C for 20 h. Cells were then harvested by centrifugation and lysed by a high-pressure homogenizer at 850 bar in the lysis buffer (100 mM Tris, pH 8.0, 200 mM NaCl, and 1 mM phenylmethylsulfonyl fluoride). Cell debris was removed by centrifugation at 21,500 rpm for 1 h. The supernatant was supplemented with 0.05% DDM and incubated with the Ni-NTA resin (GE Healthcare) for half an hour with gentle shaking. The mixture was then packed into a column, washed in turn with buffer I (100 mM Tris, pH 8.0, 200 mM NaCl, 0.02% DDM, and 20 mM imidazole) and buffer II (100 mM Tris, pH 8.0, 200 mM NaCl, 0.02% DDM, and 100 mM imidazole). The TFP complex was then eluted from the column using buffer III (100 mM Tris, pH 8.0, 200 mM NaCl, 0.02% DDM, and 200 mM imidazole) and further purified using a Superdex 200 10/300 GL column (GE Healthcare) in the gel filtration buffer (100 mM Tris, pH 8.0, 200 mM NaCl, 0.02% DDM). Fractions containing purified TFP were pooled and concentrated using an Amicon concentrator to 4 mg/mL for cryo-EM study. The TFP mutant used in the liposome binding assay was purified following a similar procedure.

TFP Activity Assay. The TFP assay measures the production of acetyl-CoA. The trans-2-enoyl-palmitoyl-CoA was enzymatically generated using purified very long-chain-specific acyl-CoA dehydrogenase (VLCAD), palmitoyl-CoA, and 2,6-dichlorophenolindophenol (DCPIP). The TFP assay was then performed in a reaction buffer containing 50 mM Tris, pH 8.5, 100 mM KCl, 100 mM $MgCl_2$, 1 mM CoA, 1 mM NAD, 0.1 mg/mL BSA, and 60 μM trans-2-enoyl-palmitoyl-CoA. The reaction was started by adding TFP (64 μg) to 100 μL of the reaction buffer and incubated at 37 °C for 10 min. At the end of the reaction, 0.33 nmol [$^{13}C_2$]-acetyl-CoA was added as the internal standard, and 600 μL of precooled methanol was added to extract the small-molecule metabolites on ice. The reaction mixture was centrifuged at 20,000 × *g* for 10 min at 4 °C. Then, 400 μL of the supernatant was taken out and mixed with 600 μL of distilled water to make 1 mL of the final sample for the measurement of acetyl-CoA by LC-MS. The LC-MS system is composed of an AB SCIEX 5500 triple-quadrupole mass spectrometer and a Shimadzu DGU-20A liquid chromatography instrument with an Agilent column. The buffer gradient is generated by 100–0% buffer A (100% water, 0.1% formic acid) and 0–100% buffer B (100% acetonitrile, 0.1% formic acid) in 10 min. The absolute concentration of acetyl-CoA is calculated by comparing the peak areas of acetyl-CoA and [$^{13}C_2$]-acetyl-CoA.

Negative Staining and Cryo-Electron Microscopy. For the negative-staining experiment, 4 μL TFP (0.1 mg/mL) was applied onto a glow-discharged carbon-coated copper grid. After ∼40 s, the grid was blotted by filter paper and stained with 2% uranyl acetate or 0.75% uranyl formate. The grids were then air dried and examined using a Tecnai T12 electron microscope (FEI) operated at 120 kV. Images were recorded using a 4 k × 4 k CCD camera (Gatan). The cryo-grids were prepared using a Vitrobot Mark IV (FEI) at 4 °C and 100% humidity. A 4-μL sample (4 mg/mL) was applied onto a glow-discharged holey-carbon gold grid (Quantifoil, R1.2/1.3, 300 mesh). After 3 s, the grids were blotted for several seconds at force 0 and dropped into the liquid ethane for quick freezing. The cryo-grids were screened using a Tecnai Arctica electron microscope (FEI) operated at 200 kV. Images were recorded with a Falcon II camera (FEI). Good grids were then recovered and transferred to a Titan Krios electron microscope (FEI) operated at 300 kV for data collection. Data acquisition was performed semiautomatically using University of California San Francisco (UCSF) Image4 in the movie mode with the defocus ranging from 1.5 to 2.5 μm. Micrographs were recorded using a K2 Summit direct electron detector (Gatan) in a superresolution mode at a nominal magnification of 22,500×, corresponding to a calibrated pixel size of 0.66 Å at object scale, with a dose rate of 8.2 counts (10.9 electrons) per pixel per second for a total exposure time of 8 s, resulting in a movie stack with 32 frames.

Image Processing. Three batches of data were collected, with 4,928 micrographs in total. Drift correction and twofold binning were applied on the superresolution movie stacks using MotionCor2 (33) and Unblur (34) with the first two frames and the last one discarded, generating summed images with or without electron-dose weighting, with a rescaled pixel size of 1.32 Å. Images with pixel size of 1.32 Å were regarded as the full-size images for following processing. The contrast transfer function (CTF) parameters for each micrograph were estimated using CTFFIND4 (35) on the basis of summed images without dose weighting. Summed images and CTF power spectra were screened manually using SPIDER (36) to exclude low-quality micrographs. About 2,000 particles were picked manually and processed with 2D classification using RELION2.0 (37). The resulting 2D averages with high quality were selected as templates to perform particle autopicking on micrographs without electron-dose weighting. For the three batches of data, 338.7 k, 711.6 k, and 489.3 k particles were extracted, respectively. Several rounds of 2D classification were performed to exclude noise and other bad particles using RELION2.0. Around 1.5 million particles corresponding to high-quality 2D averages were selected for further 3D classification using RELION2.0. The initial model was calculated from 2D averages with EMAN2 (38) based on the common line method. To separate different compositional or conformational states more thoroughly, 3D refinement was performed with the C1 symmetry after preliminary classification. Particles were recentered and reextracted from the summed images with dose weighting, based on the x, y shift and Euler angle from refinement, and processed by supervised 3D classification with different density maps from preliminary 3D classification as references. Several states were separated, including the tetramer (α2β2, 51%) and the octamer (α4β4, 26%) (*SI Appendix*, Fig. S2). To isolate octamer with higher conformational stability and to distinguish different conformational states, all nontetramer particles were merged and processed by a cascade of 3D classification. The relatively stable states of octamer were refined with a global mask by using the D2 symmetry. The resolution of batch 2 data was obviously lower than the resolution of batch 1 or batch 3. Therefore, particles corresponding to the tetramer from batch 1 and 3 data were merged and processed using the following refinement strategy: refinement on twofold binned particles with the C2 symmetry applied, refinement on full-size particles, and mask-based refinement (a global mask and a detergent-free mask). The nominal resolution of the final density map for the tetramer is 4.2 Å, based on the gold-standard Fourier shell correlation (0.143 criteria) after correction for the use of masks. The density maps were sharpened by a B-factor of −280 $Å^2$ using RELION2.0. The local resolution map was calculated using ResMap (39) and exhibited using UCSF Chimera (40).

Model Building and Structure Refinement. Initial models of TFPα and TFPβ were generated using SwissModel (41) and docked into the cryo-EM density map using Chimera. Further model building was performed using Coot (42), and refined using the real-space refinement in Phenix (43). Figures were prepared with Chimera and Pymol (Schrödinger).

Liposome Binding Assay. The 1,2,dioleoyl-sn-glycero-3-phosphocholine (DOPC) and 1,2,dioleoyl-sn-glycero-3-phosphoethanolamine (DOPE) were purchased from Avanti Polar Lipid. Cardiolipin was purchased from Sigma. Texas Red 1,2,dihexadecanoyl-sn-glycero-3-phosphoetanolamine (Texas-DHPE) was purchased from Invitrogen. They were mixed in the following mass ratio: 40% DOPC, 30% DOPE, 30% cardiolipin, and supplemented with 1% Texas-DHPE. A lipid film was formed by drying the solvent under nitrogen flow and sequentially hydrated at a final concentration of 2.5 mg/mL with buffer (100 mM Tris, pH 7.2, 200 mM NaCl). The resulting liposome suspension was frozen and thawed for 15 cycles and extruded through a polycarbonate filter (Avanti Polar Lipids) with a pore size of 400 nm. For each experiment, 24 μL of liposome was

incubated with 126 μL protein sample containing 5 μg various TFP proteins (in 100 mM Tris, pH 8.0, 200 mM NaCl, 0.02% DDM) at room temperature for 1 h. The mixtures were then adjusted to 35% Optiprep (D1556, Sigma) and overlaid with 2.5 mL of 30% Optiprep and 100 μL of buffer (100 mM Tris, pH 8.0, 200 mM NaCl). The samples were centrifuged at 49,000 rpm in a Beckman MLS-50 rotor for 2.5 h at 4 °C. After centrifugation, 200-μL aliquots were taken out at different layers, from top to bottom. The results were examined by SDS/PAGE and immunoblotting, using a rabbit anti-TFPα antibody (ab203114, Abcam) and a mouse anti-His antibody (HT501, Transgen). Detection was performed by enhanced chemiluminescence using the High-Sig ECL Western blotting substrate.

Mitochondria Isolation and Fractionation. HEK293A cells were grown in a 15-cm dish and transfected with 8 μg DNA (4 μg TFPα and 4 μg TFPβ, or 4 μg TFPα and 4 μg empty vector) using 32 μL polyethylenimine (PEI). The cells were harvested 24 h later, and the mitochondria were isolated as previously described (44). Briefly, the cells were disrupted on ice using a Dounce homogenizer in 3–4 mL IBcells-1 buffer (30 mM Tris, pH 7.4, 225 mM mannitol, 75 mM sucrose, 0.1 mM EGTA). The homogenate was centrifuged twice at 600 × *g* for 10 min, and the supernatant was further centrifuged at 7,000 × *g* for 15 min. The pellet containing the mitochondria was gently resuspended in 1 mL IBcells-2 (30 mM Tris, pH 7.4, 225 mM mannitol, 75 mM sucrose) and centrifuged again at 7,000 × *g* for 15 min. The pellet was resuspended in 1 mL IBcells-2, and centrifuged at 10,000 × *g* for 15 min. The crude mitochondrial pellet obtained was resuspended gently in 100–150 μL of mitochondria resuspending buffer (5 mM Hepes, pH 7.4, 250 mM mannitol, 0.5 mM EGTA), and lysed with a Vibra-Cell sonicator (20% amplitude, cool on ice for 10 s after every 10 strokes until the mitochondrial suspension became clear; SONICS). The resulting mixture was then first centrifuged at 10,000 × *g* for 15 min to remove the unbroken mitochondria, and the supernatant was further centrifuged at 100,000 × *g* for 1 h to separate the soluble proteins and the membrane. The distribution of different proteins was analyzed by immunoblotting with anti-COX2 (rabbit, 55070–1-AP; Proteintech), anti-LRP130 (rabbit, 21175–1-AP; Proteintech), anti-Flag (rabbit, 20543–1-AP; Proteintech), and anti-V5 (rabbit, AB3792; Millipore) antibodies.

ACKNOWLEDGMENTS. We thank the Tsinghua University cryo-EM Facility of the China National Center for Protein Sciences (Beijing) for providing resources for data collection and computation. Part of the computation was also supported by the High-Performance Computing Platform of Peking University. The work was supported by the National Key Research and Development Program of China (2017YFA0505200 and 2016YFC0906000; to J.X.), the National Science Foundation of China (31570735; to J.X.), and the Clinical Medicine Plus X Young Scholars Project of Peking University (J.X.).

1. El-Fakhri M, Middleton B (1982) The existence of an inner-membrane-bound, long acyl-chain-specific 3-hydroxyacyl-CoA dehydrogenase in mammalian mitochondria. *Biochim Biophys Acta* 713:270–279.
2. Rinaldo P, Matern D, Bennett MJ (2002) Fatty acid oxidation disorders. *Annu Rev Physiol* 64:477–502.
3. Kompare M, Rizzo WB (2008) Mitochondrial fatty-acid oxidation disorders. *Semin Pediatr Neurol* 15:140–149.
4. Knox TA, Olans LB (1996) Liver disease in pregnancy. *N Engl J Med* 335:569–576.
5. Ibdah JA, et al. (1999) A fetal fatty-acid oxidation disorder as a cause of liver disease in pregnant women. *N Engl J Med* 340:1723–1731.
6. Yang Z, Yamada J, Zhao Y, Strauss AW, Ibdah JA (2002) Prospective screening for pediatric mitochondrial trifunctional protein defects in pregnancies complicated by liver disease. *JAMA* 288:2163–2166.
7. Kantor PF, Lucien A, Kozak R, Lopaschuk GD (2000) The antianginal drug trimetazidine shifts cardiac energy metabolism from fatty acid oxidation to glucose oxidation by inhibiting mitochondrial long-chain 3-ketoacyl coenzyme A thiolase. *Circ Res* 86: 580–588.
8. Liu X, et al. (2008) Characterization of mitochondrial trifunctional protein and its inactivation study for medicine development. *Biochim Biophys Acta* 1784:1742–1749.
9. MacInnes A, et al. (2003) The antianginal agent trimetazidine does not exert its functional benefit via inhibition of mitochondrial long-chain 3-ketoacyl coenzyme A thiolase. *Circ Res* 93:e26–e32.
10. Fould B, et al. (2010) Structural and functional characterization of the recombinant human mitochondrial trifunctional protein. *Biochemistry* 49:8608–8617.
11. Fukawa T, et al. (2016) Excessive fatty acid oxidation induces muscle atrophy in cancer cachexia. *Nat Med* 22:666–671.
12. Ishikawa M, Tsuchiya D, Oyama T, Tsunaka Y, Morikawa K (2004) Structural basis for channelling mechanism of a fatty acid β-oxidation multienzyme complex. *EMBO J* 23: 2745–2754.
13. Venkatesan R, Wierenga RK (2013) Structure of mycobacterial β-oxidation trifunctional enzyme reveals its altered assembly and putative substrate channeling pathway. *ACS Chem Biol* 8:1063–1073.
14. Uchida Y, Izai K, Orii T, Hashimoto T (1992) Novel fatty acid beta-oxidation enzymes in rat liver mitochondria. II. Purification and properties of enoyl-coenzyme A (CoA) hydratase/3-hydroxyacyl-CoA dehydrogenase/3-ketoacyl-CoA thiolase trifunctional protein. *J Biol Chem* 267:1034–1041.
15. Nelson DL, Cox MM, Lehninger AL (2017) *Lehninger Principles of Biochemistry* (W.H. Freeman and Company; Macmillan Higher Education, New York), 7th Ed, p. 656.
16. Voet D, Voet JG (2011) *Biochemistry* (John Wiley & Sons, Hoboken, NJ), 4th Ed, p. 948.
17. Carpenter K, Pollitt RJ, Middleton B (1992) Human liver long-chain 3-hydroxyacyl-coenzyme A dehydrogenase is a multifunctional membrane-bound beta-oxidation enzyme of mitochondria. *Biochem Biophys Res Commun* 183:443–448.
18. Kamijo T, et al. (1994) Mitochondrial trifunctional protein deficiency. Catalytic heterogeneity of the mutant enzyme in two patients. *J Clin Invest* 93:1740–1747.
19. Orii KE, et al. (1996) Formation of the enzyme complex in mitochondria is required for function of trifunctional beta-oxidation protein. *Biochem Biophys Res Commun* 219: 773–777.
20. Boese EA, et al. (2016) Characterization of chorioretinopathy associated with mitochondrial trifunctional protein disorders: Long-term follow-up of 21 cases. *Ophthalmology* 123:2183–2195.
21. Liu J, Ghaziani TT, Wolf JL (2017) Acute fatty liver disease of pregnancy: Updates in pathogenesis, diagnosis, and management. *Am J Gastroenterol* 112:838–846.
22. Tyni T, et al. (2002) Mitochondrial fatty acid β-oxidation in the retinal pigment epithelium. *Pediatr Res* 52:595–600.
23. Tyni T, et al. (1998) Ophthalmologic findings in long-chain 3-hydroxyacyl-CoA dehydrogenase deficiency caused by the G1528C mutation: A new type of hereditary metabolic chorioretinopathy. *Ophthalmology* 105:810–824.
24. Barycki JJ, O'Brien LK, Strauss AW, Banaszak LJ (2001) Glutamate 170 of human l-3-hydroxyacyl-CoA dehydrogenase is required for proper orientation of the catalytic histidine and structural integrity of the enzyme. *J Biol Chem* 276:36718–36726.
25. Boutron A, et al. (2011) Comprehensive cDNA study and quantitative analysis of mutant HADHA and HADHB transcripts in a French cohort of 52 patients with mitochondrial trifunctional protein deficiency. *Mol Genet Metab* 103:341–348.
26. Meriläinen G, Poikela V, Kursula P, Wierenga RK (2009) The thiolase reaction mechanism: The importance of Asn316 and His348 for stabilizing the enolate intermediate of the Claisen condensation. *Biochemistry* 48:11011–11025.
27. Purevsuren J, et al. (2008) Study of deep intronic sequence exonization in a Japanese neonate with a mitochondrial trifunctional protein deficiency. *Mol Genet Metab* 95: 46–51.
28. Scheuerman O, Wanders RJA, Waterham HR, Dubnov-Raz G, Garty BZ (2009) Mitochondrial trifunctional protein deficiency with recurrent rhabdomyolysis. *Pediatr Neurol* 40:465–467.
29. Spiekerkoetter U, Khuchua Z, Yue Z, Bennett MJ, Strauss AW (2004) General mitochondrial trifunctional protein (TFP) deficiency as a result of either α- or β-subunit mutations exhibits similar phenotypes because mutations in either subunit alter TFP complex expression and subunit turnover. *Pediatr Res* 55:190–196.
30. Diekman EF, et al. (2014) Muscle MRI in patients with long-chain fatty acid oxidation disorders. *J Inherit Metab Dis* 37:405–413.
31. Spiekerkoetter U, Sun B, Khuchua Z, Bennett MJ, Strauss AW (2003) Molecular and phenotypic heterogeneity in mitochondrial trifunctional protein deficiency due to β-subunit mutations. *Hum Mutat* 21:598–607.
32. Ushikubo S, et al. (1996) Molecular characterization of mitochondrial trifunctional protein deficiency: Formation of the enzyme complex is important for stabilization of both alpha- and beta-subunits. *Am J Hum Genet* 58:979–988.
33. Zheng SQ, et al. (2017) MotionCor2: Anisotropic correction of beam-induced motion for improved cryo-electron microscopy. *Nat Method* 14:331–332.
34. Grant T, Grigorieff N (2015) Measuring the optimal exposure for single particle cryo-EM using a 2.6 Å reconstruction of rotavirus VP6. *eLife* 4:e06980.
35. Rohou A, Grigorieff N (2015) CTFFIND4: Fast and accurate defocus estimation from electron micrographs. *J Struct Biol* 192:216–221.
36. Shaikh TR, et al. (2008) SPIDER image processing for single-particle reconstruction of biological macromolecules from electron micrographs. *Nat Protoc* 3:1941–1974.
37. Kimanius D, Forsberg BO, Scheres SHW, Lindahl E (2016) Accelerated cryo-EM structure determination with parallelisation using GPUs in RELION-2. *eLife* 5:e18722.
38. Tang G, et al. (2007) EMAN2: An extensible image processing suite for electron microscopy. *J Struct Biol* 157:38–46.
39. Kucukelbir A, Sigworth FJ, Tagare HD (2014) Quantifying the local resolution of cryo-EM density maps. *Nat Methods* 11:63–65.
40. Pettersen EF, et al. (2004) UCSF Chimera–A visualization system for exploratory research and analysis. *J Comput Chem* 25:1605–1612.
41. Biasini M, et al. (2014) SWISS-MODEL: Modelling protein tertiary and quaternary structure using evolutionary information. *Nucleic Acids Res* 42:W252–W258.
42. Emsley P, Lohkamp B, Scott WG, Cowtan K (2010) Features and development of Coot. *Acta Crystallogr D Biol Crystallogr* 66:486–501.
43. Adams PD, et al. (2010) PHENIX: A comprehensive Python-based system for macromolecular structure solution. *Acta Crystallogr D Biol Crystallogr* 66:213–221.
44. Wieckowski MRMR, Giorgi C, Lebiedzinska M, Duszynski J, Pinton P (2009) Isolation of mitochondria-associated membranes and mitochondria from animal tissues and cells. *Nat Protoc* 4:1582–1590.